PCCP

Accepted Manuscript

ROYAL SOCIETY OF CHEMISTRY

www.rsc.org/pccp

Quantum chemical protocols for modeling reactions and spectra in astrophysical ice analogs: The challenging case of the $C^+ + H_2O$ reaction in icy grain mantles

David E. Woon*

Department of Chemistry

University of Illinois at Urbana-Champaign

Box 92-6, CLSL

600 S. Mathews, Urbana, IL 61801

*corresponding author

dewoon@illinois.edu

Suggested running title: Protocols for modeling ice mantle reactions

Keywords:

Icy grain mantles that accrete on refractory dust particles in the very cold interstellar medium or beyond the snow line in protoplanetary disks serve as minute incubators for heterogeneous chemistry. Ice mantle chemistry can differ significantly from the gas phase chemistry that occurs in these environments and is often richer. Modeling ices and their chemistry is a challenging task for quantum theoretical methods, but theory promises insight into these systems that is difficult to attain with experiments. Density functional theory (DFT) is predominately employed for modeling reactions in icy grain mantles due to its favorable scalability, but DFT has limitations that risk undercutting its reliability for this task. In this work, basic protocols are proposed for identifying the degree to which DFT methods are able to reproduce experimental or higher level theoretical results for the fundamental interactions upon which ice mantle chemistry depends, including both reactive interactions and non-reactive scaffolding interactions. The exemplar of this study is the reaction of C^+ with H_2O, where substantial methodological differences are found in the prediction of gas phase relative energetics for stationary points (about 10 kcal/mol for the C-O bond energy of the H_2OC^+ intermediate), which in turn casts doubt about employing it to treat the $C^+ + H_2O$ reaction on an ice surface. However, careful explorations demonstrate that B3LYP with small correlation consistent basis sets performs in a sufficiently reliable manner to justify using it to identify plausible chemical pathways, where the dominant products were found to be neutral HOC and the CO^- anion plus one and two H_3O^+ cations, respectively. Predicted vibrational and electronic spectra are presented that would serve to verify or disconfirm the pathways; the latter were computed with time-dependent DFT.

Conclusions are compared with those of a recent similar study by McBride and coworkers (*J. Phys. Chem. A*, 2014, **118**, 6991).

1. Introduction

Although carbon is the fourth most abundant element in the universe, it is rare compared to hydrogen and helium, comprising only 0.5% of the elemental abundance of the solar system.[1] Given that baryonic matter (the chemical elements) as a whole makes up only 5% of the matter and energy in the universe,[2] carbon and the other minor elements are extremely rare from a universal perspective. In spite of its scarcity, carbon-containing compounds are found in many astrophysical environments, from the interstellar and circumstellar media (ISM/CSM) to planetary atmospheres and meteorites, comets, Kuiper belt objects, and interplanetary dust.[3] Of the nearly 200 compounds identified at least tentatively to date in the ISM or CSM, a large majority of them (about 75%) contain carbon.[4] The cometary hypothesis posits that prebiotic precursors of the chemicals of life formed in the protosolar nebula were delivered to Earth's primordial surface and contributed to the emergence of terrestrial biota.[5] Rosetta instrumentation indicates that the surface of comet 67P/Churyumov-Gerasimenko is rich with organic compounds,[6] and organic compounds have been observed in many comets that have passed through the inner Solar System.

Due to the extremely cold and very low density conditions that prevail in the interstellar medium and protostellar clouds, their chemistry is dominated by barrierless exothermic reactions and by processes driven by cosmic rays and photons at ultraviolet and shorter wavelengths. When dust is present and coated with a mantle of volatile molecules—often mostly ordinary water—an alternative and potentially much richer chemistry occurs as

atoms, molecules, and ions accrete onto the ice.[7,8] Reactions that are prohibited by gas phase energetics can be very efficient on or within ice mantles.

When formed at very low temperatures, water ice is amorphous and often microporous, with a large amount of effective surface area.[9] Compaction from a microporous to a compact amorphous structure can be driven by exposure to energetic particles,[9,10] and partial compaction can occur purely thermally even at ambient cloud temperatures.[11] However, molecules near the surface in both forms of amorphous ice are not tetrahedrally coordinated and thus have both dangling H atoms and exposed O lone pairs.[12,13] The characteristics of varying ice morphologies and ice chemistry have often been probed in the laboratory at infrared wavelengths,[10-17] which is also the regime used to study ices in remote interstellar clouds.[12,16,17]

Modeling the chemistry and properties of icy grains with theoretical methods is inherently challenging because the size of the model must be large enough to correspond sufficiently with the real system to yield meaningful results. While identifying plausible pathways and predicting compositional outcomes of reactions alone can be useful to some extent for understanding ice behavior, it is preferable that theory also predict measurable properties associated with ice-bound chemistry, such as vibrational spectra. Predicting useful vibrational spectra has its own challenges, for both theoretical and experimental reasons. For the latter, the characteristic fundamental and overtone vibrational bands of water ice span much of the IR spectrum and thus hinder the identification of minor components of an ice mixture composed mostly of water.

Two strategies are in current use for modeling ice chemistry with quantum chemical methods by treating a finite cluster or periodic slab of ice: the system can be treated purely

with quantum theory, or it can be modeled with potentials that are based on quantum chemical calculations. The latter approach can be used to make infrared (IR) spectroscopic predictions for much larger systems than those that are treated directed with quantum chemical theory, but the approach is not well-suited for use when chemistry occurs or for predicting spectra in other regimes, such as electronic spectra in the ultraviolet/visible (UV-vis) region. Bowman et al.[18] recently provided a good overview of this approach.

Full quantum chemical calculations are preferable for cases where chemistry occurs, but this approach is subject to drastic limitations on the size of models that can be treated. The most accurate ab initio methodologies, such as coupled cluster theory [including the "gold standard" RCCSD(T) method[19-21]], are not usable beyond a few moieties. Density functional theory (DFT) has favorable scalability that makes it possible to study much larger cluster models than can be used with ab initio methods, but DFT results tend to be much less accurate and sometimes fail to even agree qualitatively with more rigorous methodologies. However, if it is used with care, DFT can serve very well. We have used it for treating a variety of astrochemical ice problems, such as proton transfer reactions[22-25] and addition reactions between small closed shell species.[26] Where there is reason to believe that chemistry with water in the ice is unlikely, one can also model ice behavior with a polarizable continuum model (PCM), an approach we employed to predict the electronic spectra of benzene and several small neutral polycyclic aromatic hydrocarbons (PAHs) and their cations.[27] The study in question used PCM solvation in conjunction with time-dependent DFT (TDDFT) to predict excited state energies. Our recent focus has been on the study of the low-energy deposition of cations on ice, where a number of reactions have been

found to proceed with no barrier.[28] The present study investigates the deposition of low-energy C^+ on ice.

The C^+ ion (or C II) is found in both diffuse interstellar clouds (which have extremely low density) and dense interstellar clouds (which are still lower in density than an excellent laboratory vacuum).[29,30] It is the dominant state of carbon in diffuse clouds. Although C^+ is mostly converted to CO as cloud density increases,[31] it remains an active presence, particularly in photon-dominated regions (PDRs).[32] The GOT C+ survey uses C^+ as a tracer of H_2 in clouds at the transition between clouds that are predominately atomic and clouds that are predominately molecular;[33] as these authors note, "The star formation rate in galaxies depends on how much H_2 is present in dense clouds regions in which new stars form." (p. 235). Finally, C^+ has been detected in a number of protoplanetary disks; some column density remains after subtracting the C^+ in the extended diffuse medium around the protostars.[34]

In 2008, Martinez et al.[35] reported the determination of gas phase reaction rates and product branching ratios for C^+ with five small compounds that are all known astromolecules:[4] water, ammonia, methane, acetylene, and O_2. Most of the reactions led to more complex organic products and are thus of interest both to astrochemistry and astrobiology. It is of great interest to study the analogous reactions in ice mantles, where different products are possible and even greater complexity may occur. The reaction of C^+ with pure water ice is the first step in the study of reactions of C^+ with impurities in water ice grain mantles. This reaction, however, is a particularly challenging case to use as an archetype because of the large differences that exist in the prediction of gas phase energetics between CCSD(T) and DFT methods (as we will discuss below). The level of difficulty will

be further increased by predicting both vibrational and electronic spectra of pure water ice and ice where reactions have occurred.

McBride and co-workers[36] recently published a study of the reaction of C^+ with ice that overlaps the present work to some extent and unfortunately undercuts its novelty; it followed a previous study[37] on the reaction of neutral C atom with H_2O in ice. However, sufficient differences in objectives and conclusions remain to warrant reporting our results as well. McBride and co-workers summarized the prior work on the gas phase reaction of C^+ and H_2O very well, so we will limit our remarks below to an overview. The two efforts differ in a number of ways. The present study goes beyond predicting what products are formed to predict both vibrational and electronic spectra of the ice-bound products and compares them to predicted spectra for unreacted, pure water ice to assess if any observable features are likely to be present that would confirm the predictions of the work and to distinguish the dominant products from each other. The present work is also restricted to 0 K and thus assumes minimal energy for impacting C^+ ions. This is a realistic constraint for very cold interstellar clouds. In contrast to the higher temperature ab initio molecular dynamics study of McBride et al.,[36] the present work indicates that the CO^- anion may be a persistent product at very cold temperatures.

Two experimental papers have studied the astrophysical implications of C^+ reactions with ice.[38,39] However, both of these studies utilized impact energies far beyond what has been considered in the present work or that of McBride et al.[36] The lowest irradiation energy used in these studies is about 4 keV, which is more than 20 times the amount of energy required to completely atomize the largest cluster of pure water ($19H_2O$) used in this work. Ice processing with particles with keV energies is relevant to ions found in solar and stellar wind,

magnetospheric plasmas of gas giants, and cosmic rays. The chemistry in environments exposed to such extreme irradiation is vastly different than what would be encountered in cold quiescent interstellar clouds or deep in a protoplanetary disk beyond the snow line.

As the title indicates, one emphasis of the present study is to define a basic set of protocols chosen to establish the degree to which DFT calculations are reliable for modeling ice mantle chemistry as well as for predicting vibrational and electronic spectra of ice mixtures. This is intended to be helpful for non-specialists by providing a straightforward assessment of the robustness of the ice models using experimental results as much as possible. It is standard practice to establish the reliability of quantum chemical calculations by comparing against experimental results or the results of calculations at higher levels of theory: the aim of proposing protocols here is to be as thorough as possible and to work toward establishing standards for this specialized sub-field.

In the next section, we will briefly describe the various computational methodologies that were used and the set of protocols we have established to guide this and our future studies of interstellar ice calculations. Six clusters containing from 16 to 19 H_2O molecules were optimized as a starting point for predicting spectra of pure ice and for reaction studies. Results for C^+ reacting with these clusters in various ways follow, with a description of the reaction outcomes and spectral predictions. Analysis and conclusions follow. The present study includes additional benchmark results that are largely collected as Electronic Supplemental Information (ESI) to avoid cluttering the primary narrative of the work.

2. Methodology and protocols

The DFT calculations reported in this work were performed with the Gaussian 09 program suite,[40] while coupled cluster and multireference configuration interaction

calculations were performed with the Molpro 2010 program suite.[41] Benchmark calculations were limited to three of the vast and constantly expanding multitude of available DFT functionals: the ever-popular B3LYP functional,[42-44] the X3LYP variation created by Xu and Goddard[45] and advocated by them for use with H_2O,[46] and the dispersion-corrected ωB97X-D functional of Chai and Head-Gordon.[47] We benchmarked results with standard Pople-style 6-31+G** and 6-311+G** basis sets[48-51] against (aug)-cc-pVXZ (X = D, T) correlation consistent basis sets[52,53] (brief forms of basis set designations will be used below: "AVTZ" will be substituted for aug-cc-pVTZ, while "MVDZ" indicates using the cc-pVDZ basis set on H and aug-cc-pVDZ sets on O and C). Harmonic frequency calculations were performed with Gaussian 09 in the usual way, but DFT functional-dependent scaling factors were expressly calculated for the most critical region of the water ice spectrum, the bending feature that appears near 1600 cm^{-1}. Time-dependent DFT (TDDFT)[54-56] can be used (with care) to predict electronic spectra of systems far larger than what can be treated with multireference ab initio methods. Calculations using the Tamm-Dancoff approximation (Gaussian 09 keyword TDA) as proposed and implemented by Hirata and Head-Gordon[57] were investigated but found to not yield faster computational efficiency. (Note that Gaussian 09, Revision D.01 includes a bug fix that makes it possible to perform the large memory TDDFT calculations described below.) A tighter integration grid invoked with the INT=ULTRAFINE option was used in all Gaussian 09 DFT calculations performed for this work.

Vibrational spectra were generated with the Molden program[58] using a full-width at half-maximum (FWHM) value of 20 cm^{-1} and Gaussian 09 intensities. Electronic excitation spectra were generated by expanding each reported TDDFT excited state with a gaussian

function centered at the transition energy with the computed oscillator strength and a FWHM of 0.1 eV. Depictions of geometrical structures were generated with an in-house program that writes code for the POV-Ray[59] rendering program.

The protocols described below were adopted for this work to provide an assessment of the reliability of the results. DFT and TDDFT calculations are benchmarked against experimental results, where available, or high level results computed with RCCSD(T) theory[60-63] or second-order Moller-Plesset[64] perturbation theory (MP2), with the exception of electronic transitions in monomers and dimers, which were benchmarked with MRCI+Q calculations[65-68] using an MCSCF reference wavefunction.[69,70] Equilibrium RCCSD(T) energy differences were corrected with zero-point energies calculated at the B3LYP/MVDZ level. The protocols are divided into non-reactive (scaffolding) interactions and reactive interactions. As the major component of a water ice cluster is of course water, the emphasis of scaffolding interactions is on accurately describing water pair interactions and the resulting colligative properties of clusters.

Protocol 1: Determine and report the fidelity of using DFT calculations for treating the non-reactive interactions relevant to the model system. Water and other unreacted molecules provide the structural scaffolding of the model and contribute to the net electrostatic field. For pair interactions, assessment involves both minima (binding energies) and other features of potential energy surfaces (long range behavior). Colligative behavior can be assessed against measurable spectral properties, including vibrational bands and vertical excitation energies. Very accurate water dimer binding energies are available for water at finite temperature, D_0,[71] and at equilibrium, D_e.[72] Band origins of vibrational features of the water monomer, dimer, and trimer have been measured and provide the means

to determine a scaling factor for DFT calculations of IR spectra. Experimental values of low-lying excited states of water and calculated values for the water dimer are available. See the ESI for details and references of the benchmark calculations performed for H_2O and small water oligomers with the B3LYP, X3LYP, and ωB97X-D functionals and various basis sets. The IR spectrum of amorphous water ice has been reported by Devlin et al.[14] as well as by Hornekær.[73] The UV-vis absorption spectrum for amorphous ice reported by Kobayashi[74] was used to evaluate our TDDFT predictions.

Protocol 2: Determine and report the fidelity of using DFT calculations for treating reactive behavior relevant to the model system. Gas phase behavior is a reasonable starting point for evaluating reaction energetics, but water can significantly change both energetics and even the outcomes of reactions. Gas phase and small cluster behavior can be benchmarked against RCCSD(T) or MP2 calculations both to compare energetics and assess qualitative behavior.

Protocol 3: Explore and report the dependence of reaction outcomes and spectral predictions upon cluster size and variations. It is important to assess the degree to which behavior (spectral features or energetics) converges as a function of the cluster size. It is necessary to perform enough repetition and explore sufficient different starting geometries to provide a sense of the range of possible reaction outcomes. One should describe possible deficits of the calculations (e.g., that one is unlikely to be able to perform sufficient repetitions to insure reasonable statistic weights for the various outcomes).

Protocol 4: Characterize and report the energetics and spectral properties of product species indicated by reaction studies in isolation. Multiple products are often formed in ice mantle reactions. Assessing their properties in isolation may aid in distinguishing spectral

features in the more complex mixture and also serves to identify potential methodological issues.

3. Water ice cluster models and their properties

Benchmark calculations (reported in the ESI and summarized below) were performed to assess the accuracy of various combinations of DFT functionals and basis sets for describing the water dimer pair interaction and the vibrational and electronic spectra of amorphous water ice cluster models.

For the water dimer binding energy, calculations indicate that correlation consistent basis sets are a better choice than Pople basis sets (see Table S1 in the ESI). Less basis set superposition error is introduced if correlation consistent basis sets are employed than if Pople basis sets are used because the occupied orbitals are expanded with more primitive Gaussian functions: The values of the $(H_2O)_2$ binding energy with the MVDZ basis set (as defined in the previous section) are closer to the benchmark value of 5.02 kcal/mol for D_e from Tschumper et al.[72] with all three functionals that were benchmarked than the Pople 6-31+G** and 6-311+G** basis set results. Incidentally, cluster calculations using MVDZ basis sets require about the same amount of time as calculations with Pople basis sets, since the number of contracted basis functions is about the same. Owing to fortuitous cancelation of error, the B3LYP/MVDZ value for the water dimer binding energy (D_e) is essentially the same as the benchmark value; using unscaled vibrational frequencies to adjust for zero-point vibration, the predicted value of D_0 is 0.34 kcal/mol below the benchmark value[71] of 3.16 ± 0.03 kcal/mol. All of the functionals were found to exhibit proper long range attraction (see Figure S1 in the ESI), implying that *n*-body interactions for H_2O are likely to

be described adequately by any of the functionals if a suitable basis set such as MVDZ is employed.

The expectation is that if the water dimer binding energy is being represented accurately, the properties that contribute to intermolecular interaction are also being represented accurately. This has been tested explicitly for water. Table S2 in the SI lists the computed equilibrium values of the dipole moment (μ_e) and average dipole polarizability (α_e) for H_2O with three DFT functionals and four basis sets that were benchmarked in this study and compares the results against published experimental values (at finite temperature, μ_0, α_0). There is much more dependence on basis set than on DFT functional, where very little variation is exhibited. It is observed that μ_e is overestimated much more for the two Pople basis sets than for the two correlation consistent basis sets, while α_e is underestimated in the same trend. The calculated values of μ_e and α_e at the B3LYP/AVDZ level are both in very good agreement with the experimental values, while the B3LYP/MVDZ results are slightly less accurate (which is evidently part of what the fortuitous cancellation of error is correcting).

Another consider is how well many body effects are being treated. Rather than explore this by calculating specific *n*-body energetics in the water trimer or large *n*-mers, a better test of how well many body effects are being described is to assess how accurately the methodologies perform at predicting directly observable properties that reflect *n*-body effects, such as the vibrational and electronic spectra of amorphous water ice. This will be described below.

Scaling factors used to correct computed harmonic frequencies were computed for the three functionals using experimental values of the water bending modes in the monomer,

dimer, and trimer (see Table S3 in the ESI). The scaling factors are similar for B3LYP and X3LYP (0.9824 and 0.9827, respectively) and slightly closer to 1 than the scaling factor for ωB07X-D (0.9748). The B3LYP/MVDZ scaling factor of 0.9824 is used below for frequencies under about 2500 cm^{-1} for all of the cluster calculations reported below. Vibrational bands at higher energies are not reported for the OH stretch region, which is too congested with very intense H_2O bands to be useful for identifying vibrational spectral features associated with minor components in ices where reactions have occurred.

To test the efficacy of the scaling factors, vibrational spectra were computed for one of the 16 H_2O clusters with each of the three DFT functionals over the range of 500–2000 cm^{-1} (see Figure S3 in the ESI). After scaling the computed harmonic frequencies with the scaling factor for each functional, the benchmark calculations were found to exhibit little variation in the position and shape of the composite water bending band near 1600 cm^{-1} among the different functionals. There is greater variation in the collection of overlapping low-frequency bands from 500 to 1100 cm^{-1}, but the overall appearance of the three spectra in this region is still fairly similar. These results indicate that the choice of functional is not especially critical for computing the spectra of water clusters.

A comparison between TDDFT and MRCI+Q/aug-cc-pVTZ (AVTZ henceforth) calculations for low-lying excited states of H_2O and $2H_2O$ (Figure S2 and Table S4 in the ESI) found qualitative agreement for low-lying states (5 and 10 excited states for the water monomer and dimer, respectively). The quantitative agreement varies from about 0.1 to 0.6 eV for the most part, which is a very large variation. B3LYP results tend to be lower than MRCI+Q numbers, while the opposite was observed for ωB97X-D results. As we will see below, the usefulness of TDDFT for distinguishing the electronic spectra of different

chemical pathways at this level of accuracy depends more on variations in threshold energies than it does on the specific positions and intensities of features, so the soft accuracy does not preclude the usefulness of the calculations.

Six clusters with 16 H_2O (2 cases), 17 H_2O, 18 H_2O (2 cases), and 19 H_2O were optimized; their coordinates are given in the ESI. They provide a good indication of how predicted spectral features vary with cluster size (Protocol 3) and offer a variety of binding site coordinations for reaction studies. Vibrational and electronic spectra were computed for the six clusters.

Figure 1 depicts the computed fundamental vibration spectra for each of the clusters from 500–2000 cm^{-1}. The spectra exhibit bands near 1600 cm^{-1} that are due to the H_2O bending vibrations as well a broader collection of bands between about 500 cm^{-1} and 1200 cm^{-1} that are due to librational motion associated with intermolecular interactions. All of the spectra exhibit a strong feature near 1625 cm^{-1} and a second feature past 1650 cm^{-1} that broadens the overall feature or gives it a shoulder (except for the first $16H_2O$ cluster, where the second feature is slightly more intense than the one near 1625 cm^{-1}). The lower frequency bands below 1200 cm^{-1} exhibit much less regularity. The spectrum at the bottom of Figure 1 is a simple arithmetic sum of the six individual scans. Summation naturally weights the larger clusters more while smoothing away outlier behavior such as the anomalous stronger second peak for the first $16H_2O$ cluster and a small feature near 1475 cm^{-1} that is only exhibited by the first $18H_2O$ cluster; it also averages the lower frequency features into a broad band with a well-defined maximum near 750 cm^{-1}. If the summed scan is compared against the relevant experimental spectrum of Devlin et al.[12] (Figure 1, trace d) or Hornekær[73] (Fig. 5.8), we see that the calculated spectrum provides a reasonable representation of amorphous ice spectra.

Both the experimental and theoretical spectra have bands that peak around 800 and 1650 cm^{-1}, with the former more intense than the latter. The peak positions of the water bend and libration in the calculated composite spectrum are 1620 and 725 cm^{-1}, respectively, which undershoot Hornekær's[73] values of 1650 and 803 cm^{-1} by about 30 and 75 cm^{-1}, respectively. The experimental band due to water bends is broader than the computed one but falls at a similar wavelength. There is a shallow and broad feature present in the experimental spectra centered at about 2200 cm^{-1} that's absent from the theoretical spectrum because it is due to vibrational overtones than are not treated here. As noted in the introduction, the vibration spectrum of amorphous water ice is congested with features, so for water ice with traces of other molecules there are only limited windows where features not associated with H_2O can stand out, especially if their intensities are low relative to the water bands.

Figure 2 depicts the individual predicted electronic spectra (vertical excitations) for the six clusters in the range of 6 to 10 eV. In all cases, 300 excited states were calculated with TDDFT. As in the case of the vibrational spectra., the electronic spectra of the six clusters exhibit both similarities and differences. All of the spectra exhibit a common stronger peak around 7.6 to 7.8 eV that is consistent with the $\tilde{X} \leftarrow \tilde{A}$ transition of gas phase H_2O (the equilibrium vertical excitation energy at the MRCI+Q/AVTZ level is 7.53 eV). A second peak centered at values that range between 9.2 and 9.8, is consistent with the $\tilde{X} \leftarrow \tilde{B}$ transition of gas phase H_2O (the equilibrium vertical excitation energy at the MRCI+Q/AVTZ level is 10.06 eV). As in the case of the vibrational spectra depicted in Figure 1, a summation was performed over all six electronic spectra, which is the last spectrum in Figure 2. The feature just below 8 eV stands out, while much of the other

variation contributes to a broad upslope with some peak character near 9.8 eV. Note that no excitation bands are found below 6 eV, and almost nothing below 7 eV.

The summed amorphous ice spectrum agrees qualitatively with the experimental electronic absorption spectrum reported by Kobayashi,[74] who measured the UV absorption of hexagonal crystalline and amorphous ice. The calculated initial peak falls at about 7.9 eV, which is somewhat shifted from the experimental value of about 8.6 eV. The discrepancy may be due to methodological error, or it may also be a consequence of cluster size. In any event, both liquid water and various water ice morphologies are known to exhibit a fairly high threshold before any electronic absorption occurs (e.g., Kobayashi[74] reported no absorption below 7.5 eV for amorphous ice).

In summary, vibrational and electronic spectra computed for six sample clusters with up to 19 H_2O demonstrate that the B3LYP/MVDZ level of theory yields acceptable accuracy and can be used to predict both vibrational and electronic spectra. The results also show that clusters of this size, while limited, are able to reproduce amorphous ice behavior sufficiently well to employ them for reaction studies. Protocols 1 and 3 are satisfied.

4. Reaction of C^+ with H_2O in amorphous ice

4.1. Benchmark calculations for gas phase $C^+ + H_2O$ reaction

Although the gas phase and ice-bound reactions of C^+ with H_2O are quite different, characterizing the outcomes and energetics of the gas phase reaction is an important step toward establishing the reliability of DFT calculations for the ice-bound system (protocol 2). The gas phase reaction is also the logical starting point for exploring the impact of just a few additional water molecules on the energetics and outcomes of the reaction.

As noted in the introduction, McBride et al.[36] summarized the prior experimental and theoretical studies of the $C^+ + H_2O$ gas phase reaction very well and should be consulted for its detailed discussion and extensive references to prior experimental and theoretical studies. The reaction begins with the formation of an intermediate:

$$C^+ + H_2O \rightarrow H_2OC^+ . \quad (1)$$

The C^+ ion can add to atoms or molecules through two forms of bonding. It is isoelectronic with the B atom and thus its ^2P ground state has a singly occupied 2p orbital that can form a covalent bond with another entity with at least one unpaired electron. It also has two unused 2p orbitals that can interact with a lone pair on another atom or molecule to form a dative bond, which is the means by which it adds to H_2O to form H_2OC^+. H_2OC^+ is a radical cation with most of the excess spin on the C center (the mulliken spin population on C is 0.97 at the B3LYP/AVTZ level).

Once formed in the gas phase, H_2OC^+ can either eject a neutral H atom to yield HOC^+ cation, or it can isomerize to *trans*-$HOCH^+$, which can in turn either isomerize to *cis*-$HOCH^+$ or to H_2CO^+ (the formaldehyde cation) or eject H from either heavy atom to yield HOC^+ or HCO^+. There are barriers for isomerization as well as for H eliminations, but they are all submerged well below the reactant asymptote. (See Figure S5 in the ESI for a simplified reaction diagram.) Both experiment and theoretical kinetics studies[75,76] show that the $HOC^+ + H$ asymptote is favored over the $HCO^+ + H$ asymptote even though the latter is lower in energy.

Benchmark calculations were performed for the gas phase $C^+ + H_2O$ reaction to compare B3LYP with AVTZ and MVDZ basis sets against RCCSD(T)/AVTZ (see Table S5 in the ESI). There is about a 10 kcal/mol difference in the stabilization energies of H_2OC^+ and

trans-$HCOH^+$ with respect to the reactant asymptote, and larger differences in the relative energies for the isomerization and H elimination transition states. It is thus important to confirm that B3LYP/MVDZ and RCCSD(T)/AVTZ calculations at least continue to yield the same outcomes in larger cluster calculations, which will be discussed in the next subsection.

In principle, the initial H_2OC^+ adduct could eject a proton (H^+) to yield neutral HOC rather than its cation, but this is much less energetically favorable in the gas phase: the $HOC + H^+$ product asymptote lies well above the $H_2O + C^+$ reactant asymptote, by 35.9 and 48.6 kcal/mol at the B3LYP/MVDZ and RCCSD(T)/AVTZ levels, respectively. However, we will see below that the condensed phase analog of the $HOC + H^+$ asymptote becomes very favorable when additional water is involved. It is also not energetically favorable for $HCOH^+$ to split into CH^+ and OH, breaking the CO bond. The asymptote is fairly endoergic, by 21.1 and 23.0 kcal mol at the B3LYP/MVDZ and RCCSD(T)/AVTZ levels, respectively; this is also why H abstraction from H_2O by C^+ is not a competitive process with addition-elimination.

4.2. Outcomes of $C^+ + H_2O$ reactions in amorphous ice in small and large clusters

When C^+ is added to H_2O in the presence of a second water molecule, the outcome is qualitatively different than described above for the gas phase reaction. H_2OC^+ forms but does not yield a stable complex with H_2O: it spontaneously loses a proton with no energetic barrier to yield neutral isoformyl radical, HOC, and hydronimum, H_3O^+. McBride et al.[36] performed a similar calculation. As shown in Figure 3, this behavior is observed in calculations performed from the same starting structures at both the B3LYP/MVDZ and RCCSD(T)/MVDZ levels of theory. C^+ can be added to either the proton donor water or proton acceptor water in the dimer, but the results are the same. It is quite straightforward to

understand why this occurs: the proton affinities (PAs) of H_2O and HOC are 161.9 and 129.9 kcal/mol at the B3LYP/MVDZ level, respectively, a difference of about 30 kcal/mol, so it is much more energetically favorable for the H_2O to possess the proton than HOC. For comparison, the RCCSD(T)/AVTZ predictions for the PAs of H_2O and HOC are 163.4 and 132.6 kcal/mol, respectively. As further depicted in Figure 3, water also extracted a proton from H_2OC^+ when C^+ was added to the water trimer and tetramer at the B3LYP/MVDZ level. As above, an optimization for the trimer case at the RCCSD(T)/AVTZ level confirmed the outcome of the B3LYP/MVDZ result. Although the energetics differ for B3LYP/MVDZ and RCCSD(T)/AVTZ, it is reassuring the products are the same for the reactions of C^+ with one, two, and three water structures.

Before moving on to larger clusters, an issue needs to be discussed that is particular to charged reaction systems, the possibility of charge transfer. In the gas phase, the ionization energy of the C atom (11.26 eV)[77] is substantially lower that than of water (12.65 eV),[78] so the charge transfer reaction to yield C and H_2O^+ is endoergic by about 1.4 eV or 32.3 kcal/mol. Thus, at quiescent dark interstellar cloud temperatures, the charge transfer reaction does not compete with reaction (1) above in the gas phase. However, ionization energies decrease with solvation,[79] and the reaction

$$C^+ + (H_2O)_n \rightarrow C + [(H_2O)_n]^+ \qquad (2)$$

is expected to become more favorable as n increases. In fact, Ng et al.[80] reported an ionization energy for the water dimer of 11.21 eV, and it may very well be reduced further in larger clusters. A complete study of the kinetics of C^+ interactions with ice would thus require treatment of the charge transfer outcome. However, the pragmatic issue within the scope of the present work is whether the charge can remain associated with the C center at

the beginning of its reaction with water clusters. In every case considered in this work, it does, as indicated by mulliken populations and the ensuing behavior of reactions. As with the small cluster results described above, the large clusters begin with the brief but short-lived formation of H_2OC^+. If charge transfer was taking place, one might expect to observe the behavior that occurs[81] when the water dimer is ionized: a proton transfers to one of the waters to yield a complex of H_3O^+ and OH. That was not observed in any of the calculations reported here.

C^+ was added to various binding sites in some of the large $n H_2O$ clusters described above. Figure 4 depicts the types of sites that are available in the $16H_2O(1)$ cluster, which is representative of all of the clusters. The sites range from those that are saturated with four coordinated waters (usually two that donate protons and two that accept protons) to those that only have three or two coordinated waters. In the case of the $16H_2O(1)$ cluster, only three sites have the normal full coordination. The sites with dangling O lone pairs tend to be very susceptible to C^+ addition, but addition was found to occur even to waters with saturated coordination.

A total of ten optimizations were performed using a variety of binding sites. Table 1 lists the clusters and sites types that were run and the outcomes. Performing full optimizations was time consuming, requiring in most cases hundreds of optimization steps and up to several weeks of real time, but it is essential to reach a minimum if one is to calculate vibrational frequencies. Ten optimizations does not provide sufficient statistical certainty about the frequencies of the various outcomes (a protocol 3 caveat), but it is useful for examining the trends that emerge.

Two outcomes dominated and a third was observed (see Figure 5): four of the runs yielded HOC + H_3O^+ + (*n*-2)H_2O, while five yielded CO^- + 2H_3O^+ + (*n*-3)H_2O. The final run yielded HCO + H_3O^+ + (*n*-2)H_2O. Unlike McBride et al.,[33] the present work found outcomes where CO^- was stabilized, while no outcomes with neutral CO were observed. The explanation for the occurrence of the HOC + H_3O^+ outcome is provided above, where it has been demonstrated that it can occur with only one water present and in other small water clusters. It is also straightforward to account for why HOC can lose a second proton if it is recognized that HOC is an acid that can dissociate to solvated H^+ (i.e., hydronium) and CO^- in ice (or solution) if the energetics are favorable and the products are stable. The H–OC bond energy is endoergic with respect to ground state H + CO, by 20.5 and 26.8 kcal/mol at the B3LYP/MVDZ and RCCSD(T)/AVTZ levels, respectively, which is part of why the dissociation is favorable in the present calculations. The dissociation would not occur, however, if CO^- was not stable in ice. While CO will not bind an electron in the gas phase, it can do so in ice because CO^- interacts much more strongly with water than neutral CO due to the very small dipole moment of the neutral species; this will be explored in more detail in the next section. Figure 6 depicts cases where HOC was optimized with 3H_2O and 5H_2O. Dissociation occurred spontaneously when five waters were present with the initial coordination depicted in the figure. Since performing a coupled cluster optimization on a structure of this size is computationally prohibitive, the dissociation was confirmed by rerunning from the same starting point at the MP2/MVDZ level. Note that the formyl radical, HCO, is more resilient to acid dissociation in ice because the H–CO bond energy is about 40 kcal/mol stronger than the H–OC bond energy; HCO retained its identity when optimized in the same 5H_2O environment where HOC dissociated, as shown in Figure 6.

The formyl radical was formed in one of the ten optimizations, as noted in Table 1. This optimization proceeded as in the cases where CO^- was formed, but the second proton was passed through a water molecule coordinated to both the H_3O^+ and CO^- moieties and thus transferred to the C atom to yield neutral HCO. Protons move rapidly in water matrices; once a proton is removed from H_2OC^+ to yield HOC or from HOC to yield CO^-, it is not likely to remain in the vicinity very long. HCO only formed in one of the six optimizations where CO^- was formed because the proton moved to a H_2O too far away to recombine with CO^- to form HCO.

With an understanding of what products are predicted to be formed when C^+ is deposited on ice at very cold temperatures and why they are stable, the next step is to examine the spectra of the product clusters to determine what features might be detected in suitable laboratory experiments. If present, particularly intense vibrational features could also be used to identify species in IR observations of interstellar ices

4.3. Spectroscopic predictions of processed ices

Vibrational spectra for the ten optimizations described above are shown in Figures 7 and 8 for the HOC and CO^- outcomes, respectively. All frequencies were scaled by 0.9824 as described previously. In the region of 500–2500 cm^{-1}, HOC has a bending mode and the CO stretch, which fall at 1115 and 1347 cm^{-1}, respectively, in the gas phase at the scaled B3LYP/MVDZ level. However, these features shift around quite a bit in the four cases shown in Figure 7. The bend is particularly inconsistent. The situation is even more difficult for the CO^- outcomes depicted in Figure 8, because the CO stretching mode overlaps the water bend. Note that H_3O^+ generates fairly intense bands, but it does so for both outcomes. The presence of H_3O^+ bands therefore only confirms that a reaction has taken place and

cannot help to distinguish the two outcomes. Figure 9 depicts the summed spectra for the different outcomes and compares them with the computed spectra of pure water ice. A fairly consistent H_3O^+ peak is present around 1300 cm^{-1} and other H_3O^+ features fall beyond the water bending feature.

Electronic spectra offer a better means for distinguishing the outcomes from each other. Figures 10 and 11 show the individual spectra for the two cases, where 200 excited states were calculated with TDDFT for each of the ten outcome structures. Both HOC and CO^- outcomes exhibit excitations below the threshold noted above for pure water clusters. At the B3LYP/MVDZ level, the excitations extend down to about 4 eV for HOC outcomes and down to about 2 eV for CO^- outcomes. Figure 12 depicts the summed spectra for the different outcomes and contrasts them with the computed spectrum of pure water amorphous ice. As above, summation reinforces the stronger features in the individual cases. The biggest difference between the two dominant outcomes is that the clusters with CO^- consistently exhibit excitations at much lower energies than the clusters with HOC. The summation spectrum for HOC outcomes exhibits two stronger peaks, at about 5.1 and 5.9 eV, while the summation spectrum for CO^- outcomes exhibits one stronger peak at about 6.2 eV. These three features are all evident in Figure 12(c), which is the summation over all ten outcomes. Based on the large discrepancy between our prediction and the experimental spectrum for our water amorphous ice, it is likely these peaks will be shifted to some extent.

The comparison of vibrational and electronic spectra indicates that both regimes would exhibit features that are not present in pure water amorphous ice, but it appears that only electronic spectroscopy could be used to distinguish the features from the two dominant outcomes. Electronic spectroscopy is not applied to the study of astrophysical ices to the

extent that vibrational spectroscopy is applied, but the present results suggest that it may provide a very useful additional probe of ice chemistry.

5. Products in Isolation – Protocol 4 Assessment

To satisfy the fourth protocol described in section 2, we will briefly examine the energetics and spectral predictions of the dominant product species in isolation, specifically HOC, CO^-, and H_3O^+. In addition to providing additional verification that B3LYP/MVDZ calculations are sufficiently accurate for treating C^+ reactions with amorphous ice models, additional issues are addressed by these calculations.

The isoformyl radical was produced in nearly half of the ten optimizations that were performed. It is straightforward to understand that the larger value of the proton affinity of H_2O drives the loss of H^+ from the initially formed H_2OC^+ adduct to form neutral HOC. HOC was found to be stable in all small clusters with four or fewer waters and in larger clusters where removing a second proton to form CO^- is not favorable due to the environment of water molecules around HOC. However, at least one coordination with five H_2O is sufficient to induce CO^- formation at both the B3LYP/MVDZ and MP2/MVDZ levels, as shown above. Figure 13(a) depicts two HOC–$n$$H_2O$ clusters (n = 1,3) not shown elsewhere. The equilibrium pair binding energy was computed for the n = 1 case: ΔE_e is -9.5 kcal/mol at the B3LYP/MVDZ level and -10.2 kcal/mol at the RCCSD(T)/AVTZ level (with no counterpoise correction in either calculation). This is similar to what was observed above for the H_2O dimer binding energy, where the RCCSD(T) result was slightly lower than the B3LYP value. The scaled B3LYP/MVDZ values of the CO stretch and H-O-C bend for gas phase HOC are 1347 and 1115 cm^{-1}, respectively, which can be compared against the very

accurate anharmonic frequencies reported recently for HOC by Morgan and Fortenberry[82] of 1366.0 and 1122.2 cm^{-1}, respectively (variational CI results are given; variational second-order perturbation theory results are similar). The B3LYP result for the CO stretch is about 20 cm^{-1} low, while the H-O-C bend is within 10 cm^{-1}. The calculated electronic spectra of the two HOC–3H_2O clusters depicted in Figures 6 and 13(a) are shown at the bottom of Figure 10 and indicate that all of the clusters with HOC, small and large, exhibit notable features as low as about 4 eV but no lower. Gas phase HOC has a low-lying excitation from the $^2A'$ ground state to the first $^2A''$ state. The B3LYP prediction for the equilibrium vertical excitation energy of 1.07 eV agrees fairly well with RCCSD(T)/AVTZ and MRCI+QAVTZ results of 0.91 and 0.90 eV, respectively. The B3LYP oscillator strength is 0.0000, however, and the MCSCF transition dipole moment is just 0.05 D, so the excitation is extremely weak. It appears in similar manner in the 1H_2O and two 3H_2O B3LYP cluster calculations, with an energy around 1 eV and negligible oscillator strength. With no other intervening excitation, the effective threshold for detectably exciting HOC in both the gas phase and in ice is around 4 eV, as noted above.

The second notable product produced in the large cluster calculations is the CO^- anion, where the formation is driven by the weak nature of the H–OC bond and the stability of the product ions, CO^- and H_3O^+. CO^- is not stable in the gas phase or small water clusters, so the pair binding energy with H_2O is not a useful benchmark to characterize. It is of far greater usefulness to characterize the relative energies of CO and CO^- in clusters with an increasing number of waters to verify if CO^- is truly more stable in ice than CO. Figure 13(b) depicts the structures of clusters with 1, 2, 4, and 6 H_2O, while Figure 14 depicts the relative energies computed in two ways. The clusters were optimized at the B3LYP/MVDZ level, and single

point energies were then computed at the RCCSD(T)/MVDZ level (the reduction in basis set quality from AVTZ to MVDZ is due to the cost of performing the 4 and 6 H_2O calculations). As shown in Figure 14, CO^- is not bound with respect to CO in optimized clusters at the B3LYP level until 4 H_2O are present, and it is not bound under these circumstances with RCCSD(T) even when 6 H_2O are present. However, the energetics of optimized clusters is not the best way to consider the stability of CO^-. While the CO and CO^- clusters are similar for 1 and 2 H_2O, the optimized structures of the complexes of CO and CO^- are quite different for 4 and 6 H_2O because CO interacts weakly with H_2O and CO^- interacts strongly with H_2O. The lower part of Figure 14 shows the vertical attachment energies for adding an electron to the $CO^- - nH_2O$ clusters. Without relaxation, CO^- is bound quite strongly, by 20 kcal/mol or more, with respect to CO when 4 and 6 H_2O are present with both B3LYP and RCCSD(T). There is no experimental observation of the CO^- vibrational frequency to use as a benchmark. Figure 11 includes the prediction of the electronic spectrum of $CO^- - 4H_2O$, showing that there are excitations as low as about 2 eV, as observed in the five large cluster optimizations that produced CO^-.

The final product is H_3O^+, a species that has received much attention from both theory and experiment in water clusters (particularly for the $n = 1$ case). The computed equilibrium energies for forming $H_5O_2^+$ from H_3O^+ and H_2O [see Figure 13(c)] are -35.8 and -34.1 kcal/mol for B3LYP/MVDZ and RCCSD(T)/AVTZ, respectively, which is again very reasonable agreement. Two vibrational modes of gas phase H_3O^+ fall in the mid IR. The agreement is very good for the ν_4 deformation mode, where the scaled B3LYP result is 1632 cm^{-1} and the experimental values of Gruebele et al.[83] are 1629.95 and 1638.55 cm^{-1}. The agreement for the umbrella mode is disappointing: 807 cm^{-1} with B3LYP is over 150

cm^{-1} off from the experimental value of 954.2 cm^{-1} of Haese and Oka.[84] Gas phase H_3O^+ does not have any excitations that fall below the threshold for H_2O excitation: the first excited state predicted by B3LYP TDDFT calculations is 11.34 eV. A 20 state calculation in the $H_3O^+ - 4H_2O$ cluster depicted in Figure 13(c) also shows no excitations under 8 eV. Thus, the low lying excitations in Figures 10 and 11 can be attributed to HOC or CO^- without the presence of H_3O^+, which is opposite of the vibrational behavior.

6. Concluding Summary

In this work the reactive behavior of the C^+ cation with amorphous ice has been with characterized with model cluster calculations. Through the use of various protocols, it has been demonstrated that B3LYP/MVDZ results are sufficiently accurate to yield reliable insight into what reaction outcomes are possible at very cold temperatures. The protocols are also useful for establishing the reliability of spectral predictions, which is a critically important capability if theoretical predictions about reaction outcomes are to be verified with subsequent experimental study. The two dominant outcomes of C^+ reactions with H_2O in ice are the HOC radical and CO^- radical anion as well as H_3O^+. It was noted that vibrational spectra would reflect that reactions had occurred due to the formation of H_3O^+, but it would not be able to distinguish between HOC and CO^- formation. The use of electronic spectra, however, would make it possible to identify if CO^- is formed, since the threshold for excitation is about 2 eV lower in energy that is the case for HOC. To the best of our knowledge, this is the first effort to predict electronic spectra of realistic ice chemistry models for interstellar ice analogs.

Acknowledgements

Funding from the NASA Exobiology and Astrobiology program (grant NNX10AR82G) is gratefully acknowledged. Dr. Lina Chen performed some of the initial calculations of CO and CO^- in water clusters.

References

1 K. Lodders, *Astrophys. J.*, 2003, **591**, 1220.

2 G. Hinshaw, D. Larson, E. Komatsu, D. N. Spergel, C. L. Bennett, J. Dunkley, M. R. Nolta, M. Halpern, R. S. Hill, N. Odegard, et al., *Astrophys. J. Supp. Ser.* 2013, **208**, 19; see also http://wmap.gsfc.nasa.gov/universe/uni_matter.html.

3 T. Henning and F. Salama, *Science*, 1998, **282**, 2204.

4 See www.astrochymist.org for a list of observed astromolecules and references for their initial detections.

5 C. F. Chyba, P. J. Thomas, L. Brookshaw, and C. Sagan, *Science*, 1990, **249**, 366.

6 F. Capaccioni, A. Coradini, G. Filacchione, S. Erard, G. Arnold, P. Drossart, M. C. De Sanctis, D. Bockelee-Morvan, T. Capria, F. Tosi, et al., *Science*, 2015, **347**, aaa0628-1.

7 R. T. Garrod, S. L. Widicus Weaver, and E. Herbst, *Astrophys. J.*, 2008, **682**, 283.

8 E. Herbst and E. F. van Dishoeck, *Annu. Rev. Astron Astrophys.*, 2009, **47**, 427.

9 U. Raut, B. D. Teolis, M. J. Loeffler, R. A. Vidal, M. Famá, and R. A. Baragiola, *J. Chem. Phys.*, 2007, **126**, 244511.

10 C. Mejía, A. L. F. de Barros, E. Seperuelo Duarte, E. F. da Silveira, E. Dartois, A. Domaracka, H. Rothard, and P. Boduch, *Icarus*, 2015, **250**, 222.

11 K. Isokoski, J.-B. Bossa, T. Triemstra, and H. Linnartz, *Phys. Chem. Chem. Phys.*, 2014, **16**, 3456.

12 M. E. Palumbo, *J. Phys. Conf. Ser.*, 2005, **6**, 211.

13 J. P. Devlin, *J. Geophys. Res.*, 2001, **106**, 33333.

14 J. P. Devlin, J. Sadlej, and V. Buch, *J. Phys. Chem. A*, 2001, **105**, 974.

15 U. Buontempo, *Phys. Lett.*, 1972, **42A**, 17.

16 W. Hagen, A. G. G. M. Tielens, and J. M. Greenberg, *Chem. Phys.*, 1981, **56**, 367.

17 E. Mayer and R. Pletzer, *Nature*, 1986, **319**, 298.

18 J. M. Bowman, Y. Wang, H. Lie, and J. S. Mancini, *J. Phys. Chem. Lett.*, 2015, **6**, 366.

19 T. L. Lee and G. E. Scuseria, In Quantum Mechanical Electronic Structure Calculations with Chemical Accuracy (S. R. Langhoff, Ed.), Kluwer Academic Publishers, Dordrecht, The Netherlands, 47-108, 1995.

20 R. J. Bartlett and M. Musial, *Rev. Mod. Phys.*, 2007, **79**, 291.

21 J. Řezáč and P. Hobza, *J. Chem. Theory Comput.*, 2013, **9**, 2151.

22 J.-Y. Park and D. E. Woon, *Astrophys. J.*, 2004, **601**, L63.

23 J.-Y. Park and D. E. Woon, *J. Phys. Chem. A*, 2004, **108**, 6589.

24 J.-Y. Park and D. E. Woon, *Astrophys. J.*, 2005, **648**, 1285.

25 D. E. Woon, *Comp. Theor. Chem.*, 2012, **984**, 108.

26 L. Chen and D. E. Woon, *J. Phys. Chem. A*, 2011, **115**, 5166.

27 D. E. Woon and J.-Y. Park, *Astrophys. J.*, 2004, **607**, 342.

28 D. E. Woon, *Astrophys. J.*, 2011, **728**, 44.

29 W. D. Langer, T. Velusamy, J. L. Pineda, P. F. Goldsmith, D. Li, and H. W. Yorke, *Astron. Astrophys.*, 2010, **521**, L17.

30 P. Bryans, H. Kreckel, E. Roueff, V. Wakelam, and D. W. Savin, *Astrophys. J.*, 2009, **694**, 286.

31 T. Snow and B. J. McCall, *Annu. Rev. Astron. Astrophys.*, 2006, **44**, 367.

32 D. J. Hollenbach and A. G. G. M. Tielens, *Annu. Rev. Astron. Astrophys.*, 1997, **35**, 179.

33 T. Velusamy, W. D. Langer, K. Willacy, J. L. Pineda, and P. F. Goldsmith, in *Molecular Gas, Dust, and Star Formation in Galaxies, Proceedings IAU Symposium No. 292* (T. Wong and J Otts., Eds.), 2013 (Cambridge University Press, Cambridge UK), 235.

34 D. Fedele, S. Bruderer, E. F. van Dishoeck, J. Carr, G. J. Herczeg, C. Salyk, N. J. Evans II, J. Bouwman, G. Meeus, T. Henning, et al., *Astron. Astrophys.* 2013, **599**, A77.

35 O. Martinez, Jr., N. B. Betts, S. M. Villano, N. Eyet, T. P. Snow, and V. M. Bierbaum, *Astrophys. J.*, 2008, **686**, 1486.

36 E. J. McBride, T. J. Millar, and J. J. Kohanoff, *J. Phys Chem. A*, 2014, **118**, 6991.

37 E. J. McBride, T. J. Millar, and J. J. Kohanoff, *J. Phys Chem. A*, 2013, **117**, 9666.

38 G. Strazzulla, G. Leto, O. Gomis, and M. A. Satorre, *Icarus*, 2003, **164**, 163.

39 A. Dawes, A. Hunniford, P D. Holtom, R. J. Makerji, R. W. McCullough, and N. J. Mason, *Phys. Chem. Chem. Phys.*, 2007, **9**, 2886.

40 M. J. Frisch, G. W. Trucks, H. B. Schlegel, G. E. Scuseria, M. A. Robb, J. R. Cheeseman, G. Scalmani, V. Barone, B. Mennucci, G. A. Petersson, et al. *Gaussian 09, Revision D.01*, Gaussian, Inc., Wallingford, CT, 2013.

41 H.-J. Werner, P. J. Knowles, G. Knizia, F. R. Manby, M. Schütz, P. Celani, T. Korona, R. Lindh, A. Mitrushenkov, G. Rauhut, et al. *Molpro 2010, Version 2010.1*, University College Cardiff Consultants Limited, 2008.

42 A. D. Becke, *J. Chem. Phys.*, 1993, **98**, 5648.

43 C. Lee, W. Yang, and R. G. Parr, *Phys. Rev. B.*, 1988, **37**, 785.

44 P. J. Stephens, F. J. Devlin, C. F. Chabalowski, and M. J. Frisch, *J. Phys. Chem.*, 1994, **98**, 11623.

45 X. Xu and W. A. Goddard III, *Proc. Nat. Acad. Sci.*, 2004, **101**, 2673.

46 X. Xu and W. A. Goddard III, *J. Phys, Chem. A*, 2004, **108**, 2305.

47 J.-D. Chai and M. Head-Gordon, *Phys. Chem. Chem. Phys.*, 2008, **10**, 6615.

48 W. J. Hehre, R. Ditchfield, and J. A. Pople, *J. Chem. Phys.*, 1972, **56**, 2257.

49 P. C. Hariharan and J. A. Pople, *Theor. Chim. Acta*, 1973, **28**, 213.

50 T. Clark, J. Chandrasekhar, G. W. Spitznagel, G. W. and P. v. R. Schleyer, *J. Comput. Chem.*, 1983, **4**, 294.

51 K. Raghavachari, J. S. Binkley, R. Seeger, and J. A. Pople, *J. Chem. Phys.*, 1980. **72**. 650.

52 T. H. Dunning, Jr., *J. Chem. Phys.*, 1989, **90**, 1007.

53 R. A. Kendall, T. H. Dunning, Jr., and R. J. Harrison, *J. Chem. Phys.*, 1992, **96**, 6796.

54 R. Bauernschmitt and R. Ahlrichs, *Chem. Phys. Lett.*, 1996, **256**, 454.

55 M. E. Casida, C. Jamorski, K. C. Casida, and D. R. Salahub, *J. Chem. Phys.*, 1998, **108**, 4439.

56 R. E. Stratmann, G. E. Scuseria, and M. J. Frisch, *J. Chem. Phys.*, 1998, **109**, 8218.

57 S. Hirata and M. Head-Gordon, *Chem. Phys. Lett.*, 1999, **314**, 291.

58 G. Schaftenaar and J. H. Noordik, *J. Comput.-Aided Mol. Design*, 2000, **14**, 123.

59 Persistence of Vision Pty. Ltd., Williamstown, Victoria, Australia, Version 3.6. http://www.povray.org/.

60 G. D. Purvis III and R. J. Bartlett, *J. Chem. Phys.*, 1982, **76**, 1910.

61 K. Raghavachari, G. W. Trucks, J. A. Pople, and M. Head-Gordon, *Chem. Phys Lett.*, 1989, **157**, 479.

62 J. D. Watts, J. Gauss, and R. J. Bartlett, *J. Chem. Phys.*, 1993, **98**, 8718.

63 P. J. Knowles, C. Hampel, and H.-J. Werner, *J. Chem. Phys.*, 1993, **99**, 5219.

64 C. Møller and M. S. Plesset, *Phys. Rev.*, 1934, **46**, 618.

65 H.-J. Werner and P. J. Knowles, *J. Chem. Phys.*, 1988, **89**, 5803.

66 P. J. Knowles and H.-J. Werner, *Chem. Phys. Lett.*, 1988, **145**, 514.

67 S. R. Langhoff and E. R. Davidson, *Int. J. Quantum Chem.*, 1974, **8**, 61.

68 E. R. Davidson and D. W. Silver, *Chem. Phys. Lett.*, 1977, **52**, 403.

69 H.-J. Werner and P. J. Knowles, *J. Chem. Phys.*, 1985, **82**, 5053.

70 P. J. Knowles and H.-J. Werner, *Chem. Phys. Lett.*, 1985, **115**, 259.

71 B. E. Rocher-Casterline, L. C. Ch'ng. A. K. Mollner, and H. Reisler, *J. Chem. Phys.*, 2011, **134**, 211101.

72 G. S. Tschumper, M. L. Leininger, B. C. Hoffman, E. F. Valeev, H. F. Schaefer III, and M. Quack, *J. Chem. Phys.*, 2002, **116**, 690.

73 L. Hornekær, in *Laboratory Astrochemistry: From Molecules through Nanoparticles to Grains* (Eds. S. Schlemmer, T. Giesen, H. Mutsche, and C. Jäger), 2015, Wiley-VCH Verlag & Co. Chapter 8, pp. 274-275.

74 K. Kobayashi, *J. Phys. Chem.*, 1983, **87**, 4317.

75 D. M. Sonnenfroh, R. A. Curtis, and J. M. Farrar, *J. Chem. Phys.*, 1985, **83**, 3958.

76 J. R. Flores and A. B. González, *J. Chem. Phys.*, 2008, **128**, 144310.

77 D. R. Lide (Ed.), *Handbook of Chemistry and Physics*, 1992, 10-211, CRC Press, Cleveland Ohio.

78 J. B. Snow and T. F. Thomas, *Int. J. Spectrom. Ion Proc.*, 1990, **96**, 49.

79 D. E. Woon, *Adv. Space. Res.*, 2004, **33**, 44.

80 C. Y. Ng, D. J. Trevor, P. W. Tiedemann, S. T. Creyer, P. L. Kronebusch, B. H. Mahan, and Y. T. Lee, *J. Chem. Phys.*, 1977, **67**, 4235.

81 O. Svoboda, D, Hollas, M. Ončák, and P. Slavícek, *Phys. Chem. Chem. Phys.*, 2013, **15**, 11531.

82 W. J. Morgan and R. C. Fortenberry, *Spectrochim. Acta A*, 2015, **135**, 965.

83 M. Gruebele, M. Polak, and R. J. Saykally, *J. Chem. Phys.*, 1987, **87**, 3347.

84 N. N. Haese and T. Oka, *J. Chem. Phys.*, 1985, **80**, 572.

Table 1 Optimization outcomes for reactions of C^+ with nH_2O clusters at various sites

Outcome	Cluster–case	Site type[a]
$HOC + H_3O^+ + (n–2)H_2O$	$16H_2O(1)–1$	ddaa
	$17H_2O(1)–2$	da
	$18H_2O(1)–2$	ddaa
	$18H_2O(2)–1$	ddaa
$CO^- + 2H_3O^+ + (n–3)H_2O$	$16H_2O(1)–2$	dda
	$17H_2O(1)–1$	dda
	$18H_2O(1)–1$	dda
	$18H_2O(1)–3$	ddaa
	$18H_2O(2)–2$	ddaa
$HCO + H_3O^+ + (n–2)H_2O$	$18H_2O(2)–3$	dda

[a] coordination environment of water where C^+ reacts; "d" and "a" indicate proton donor and proton acceptor interactions, respectively.

FIGURE CAPTIONS

Fig. 1 Predicted scaled vibrational spectra of nH_2O clusters (n = 16–19) from 500–2000 cm^{-1} obtained at the B3LYP/MVDZ level, including summation of the individual spectra.

Fig. 2 Predicted electronic spectra of nH_2O clusters (n = 16–19) through 10 eV obtained at the B3LYP/MVDZ level with TDDFT, including summation of the individual spectra.

Fig. 3 Starting structures and products for $C^+ + nH_2O$ (n = 2–4) reactions.

Fig. 4 $16H_2O$ cluster showing various saturated and unsaturated coordination sites, where *a* and *d* indicate proton acceptor and proton donor interactions, respectively: green highlight, *ddaa*; blue highlight, *dda*; orange highlight, *daa*; maroon highlight, *da*; rose, *daaa*.

Fig. 5 Sample outcomes of the reaction of C^+ with nH_2O clusters. (a) $HOC + H_3O^+ + (n\text{-}2)H_2O$ (b) $CO^- + 2H_3O^+ + (n\text{-}3)H_2O$ (c) $HCO + H_3O^+ + (n\text{-}2)H_2O$

Fig. 6 Small cluster optimizations of HOC and HCO. (a) HOC is stable with $3H_2O$ (b) HOC loses a proton to $5H_2O$ to yield $CO^- + H_3O^+ + 4H_2O$ (c) HCO is stable with $5H_2O$

Fig. 7 Predicted scaled vibrational spectra of $C^+ + nH_2O$ reactions with $HOC + H_3O^+$ products from 1000–2000 cm^{-1} obtained at the B3LYP/MVDZ level; "b" indicates the HOC bend, "s" indicates the CO stretch of HOC, and "+" indicates an H_3O^+ mode.

Fig. 8 Predicted scaled vibrational spectra of $C^+ + nH_2O$ reactions with $CO^- + 2H_3O^+$ products from 1000–2000 cm^{-1} obtained at the B3LYP/MVDZ level; "+" indicates an H_3O^+ mode.

Fig. 9 Various summations of scaled vibrational spectra compared against the summed pure water spectrum of Fig. 1 (a) summation of the four $HOC + H_3O^+$ outcomes in Fig. 5 (b) summation of the five $CO^- + 2H_3O^+$ outcomes from Fig. 6 (c) summation of all ten outcomes.

Fig. 10 Predicted electronic spectra of $C^+ + nH_2O$ reactions with $HOC + H_3O^+$ products from 4–8 eV obtained at the TDDFT B3LYP/MVDZ level.

Fig. 11 Predicted electronic spectra of $C^+ + nH_2O$ reactions with $CO^- + 2H_3O^+$ products from 2–8 eV obtained at the TDDFT B3LYP/MVDZ level.

Fig. 12 Various summations of electronic spectra compared against the summed pure water spectrum of Fig. 2 (a) summation of the four $HOC + H_3O^+$ outcomes in Fig. 5 (b) summation of the five $CO^- + 2H_3O^+$ outcomes from Fig. 6 (c) summation of all ten outcomes.

Fig. 13 Structures of product species with nH_2O. (a) HOC (b) CO/CO^- (c) H_3O^+

Fig. 14 Electron affinities (with ZPE corrections, EA_0) and vertical attachment energies (equilibrium, VAE_e) for CO/CO^- with nH_2O

Fig. 1

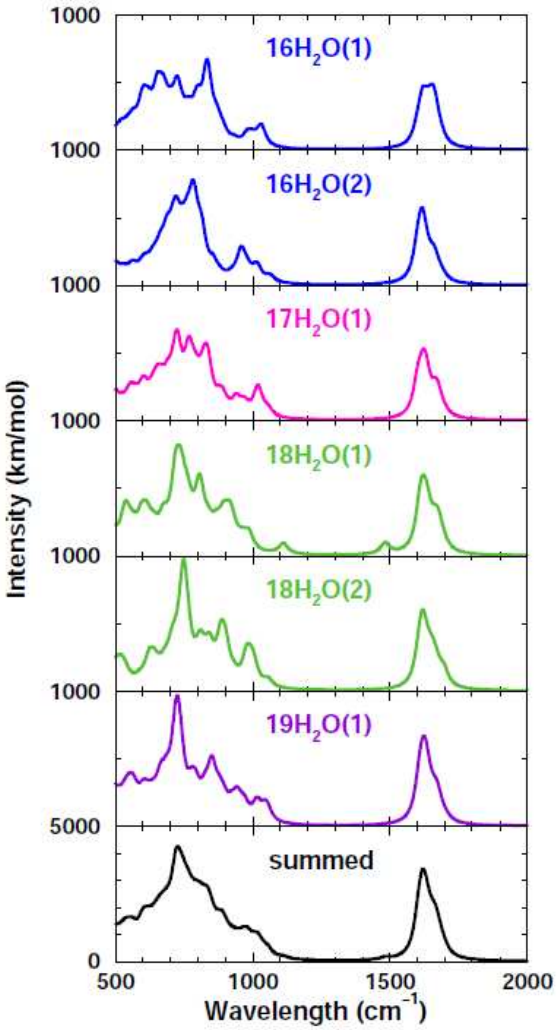

Fig. 2

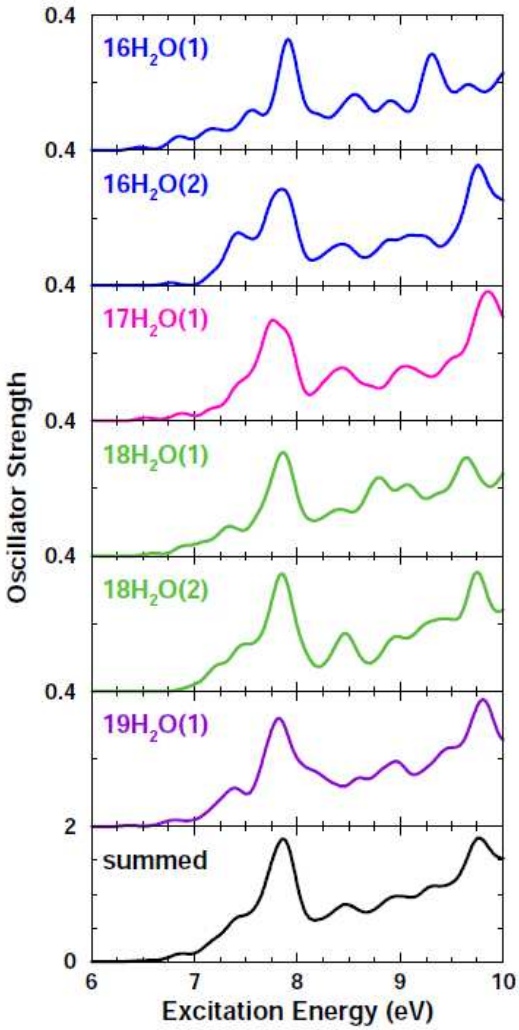

Fig. 3

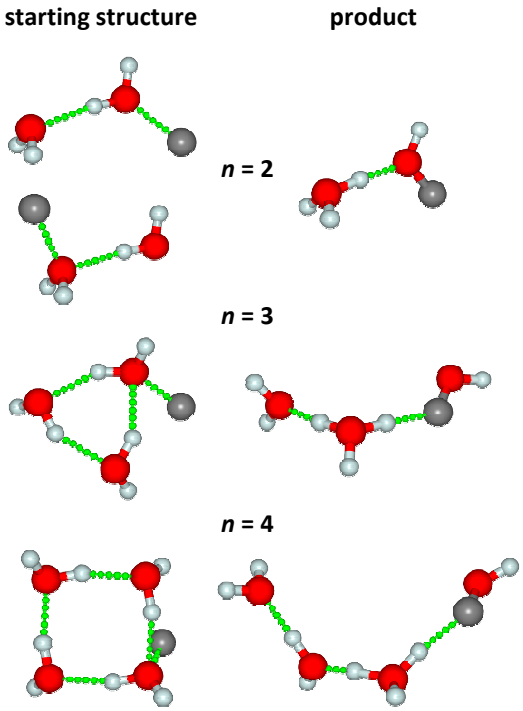

Fig. 4

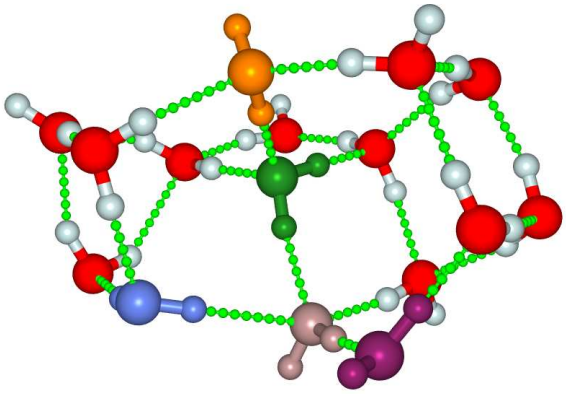

Fig. 5

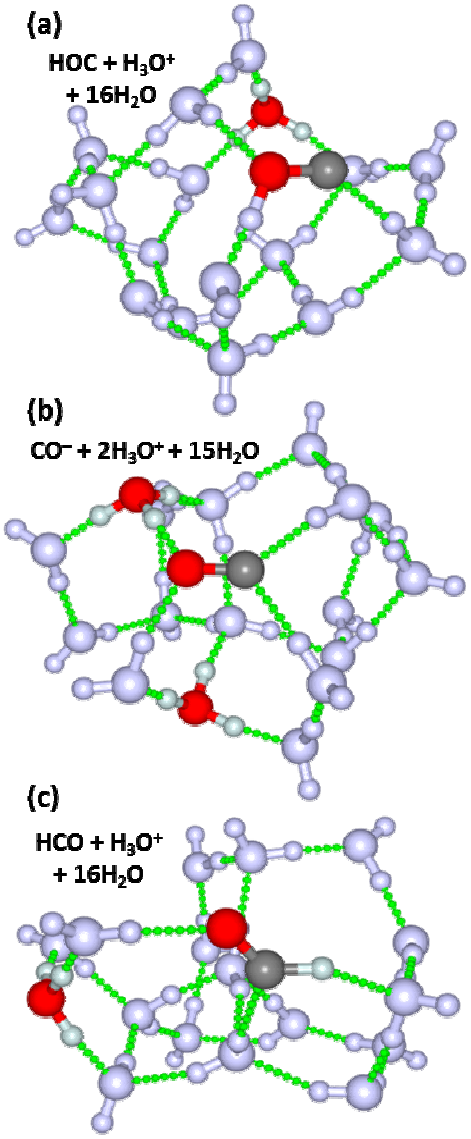

Fig. 6

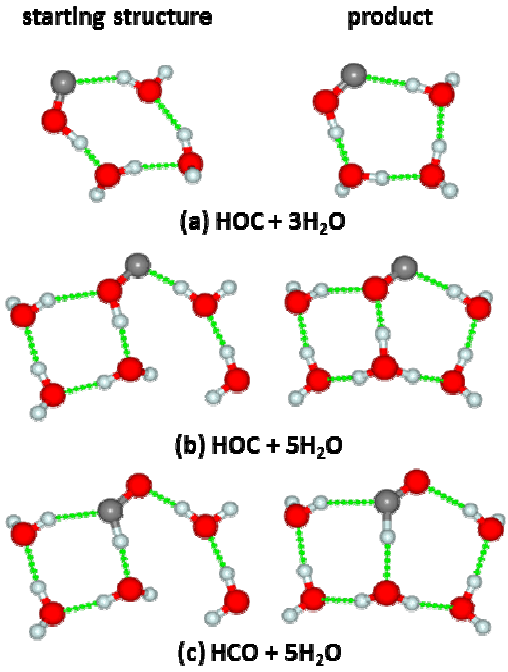

Fig. 7

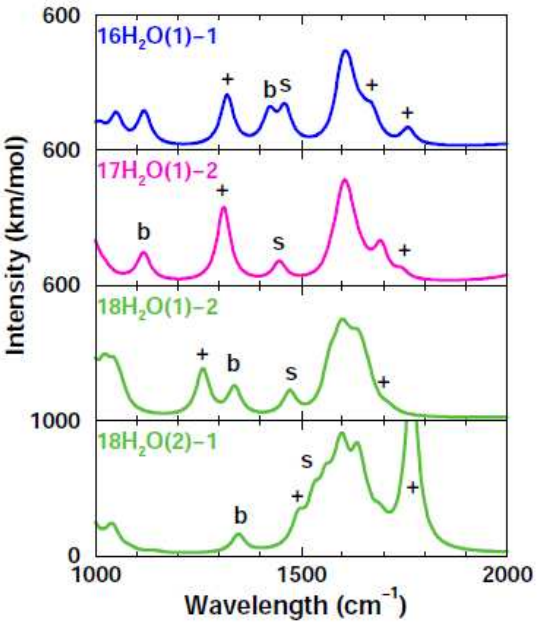

Fig. 8

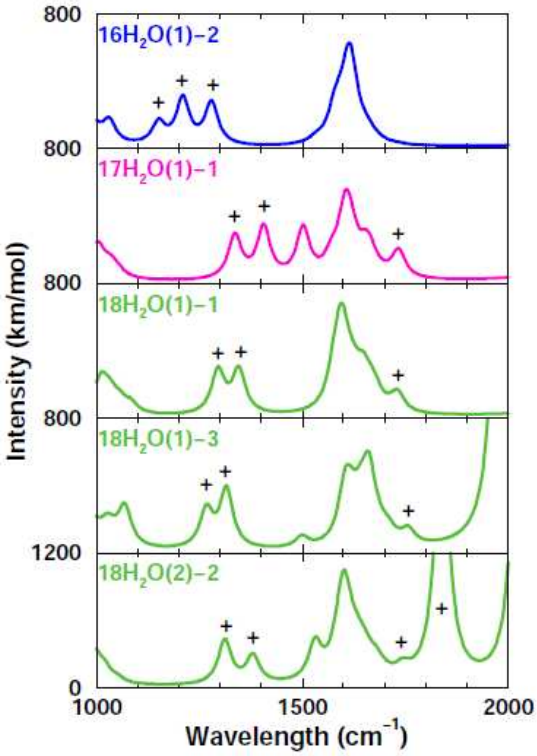

Fig. 9

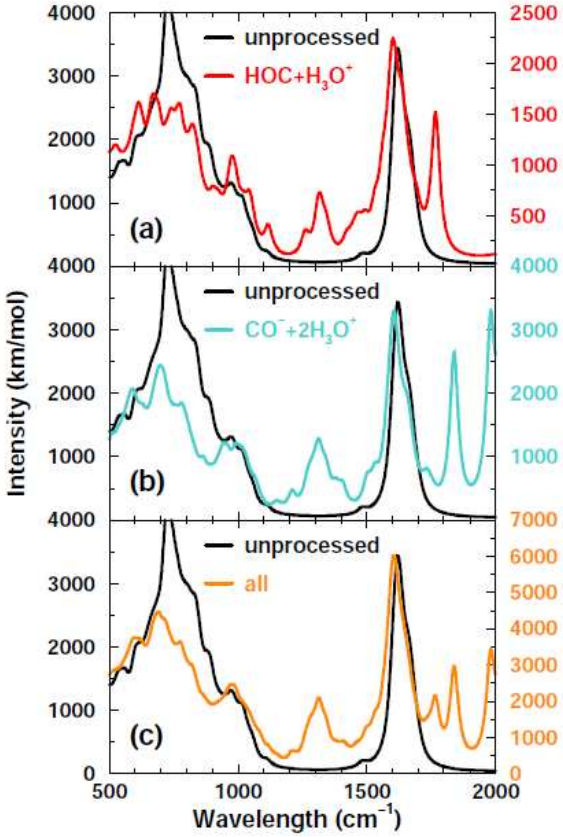

Fig. 10

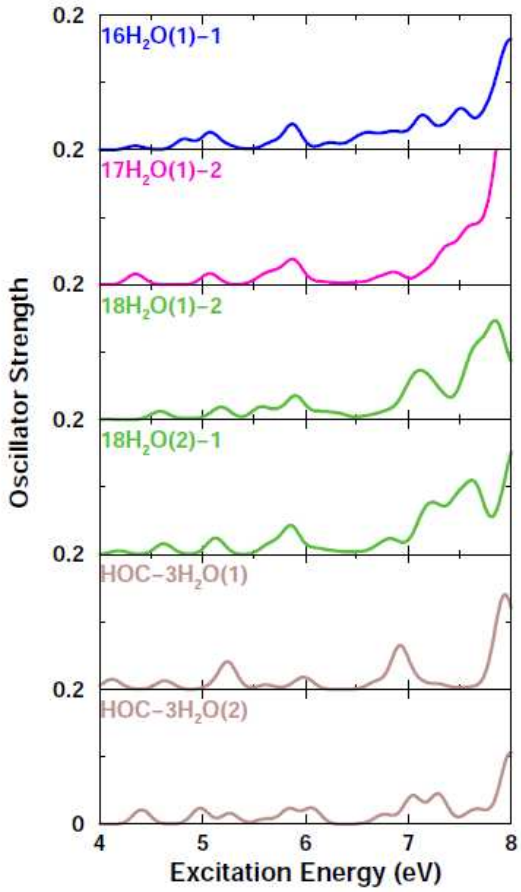

Fig. 11

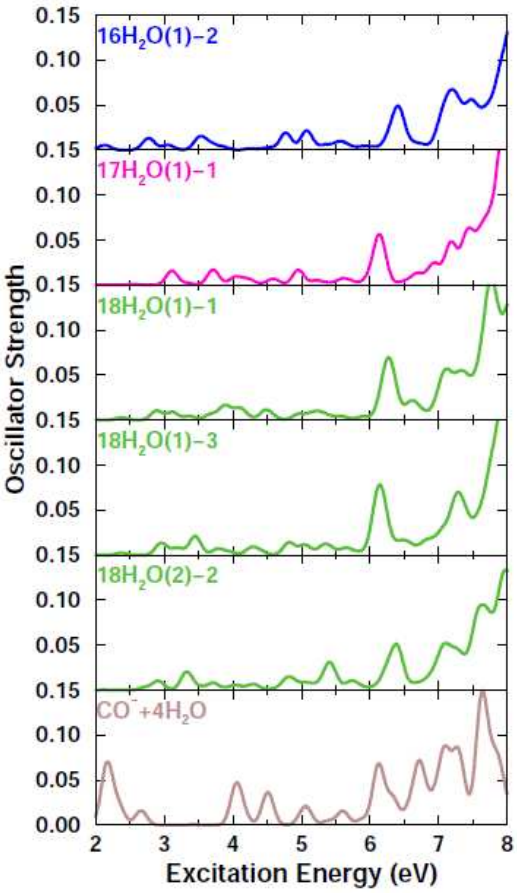

Fig. 12

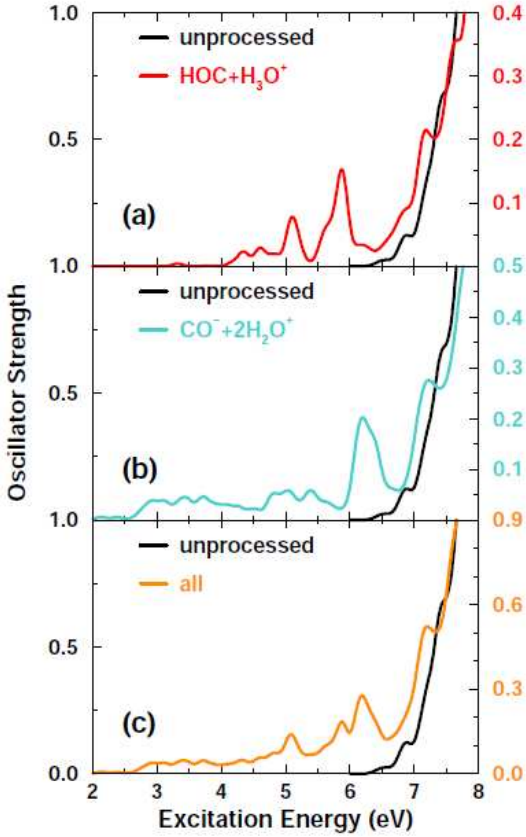

Fig. 13

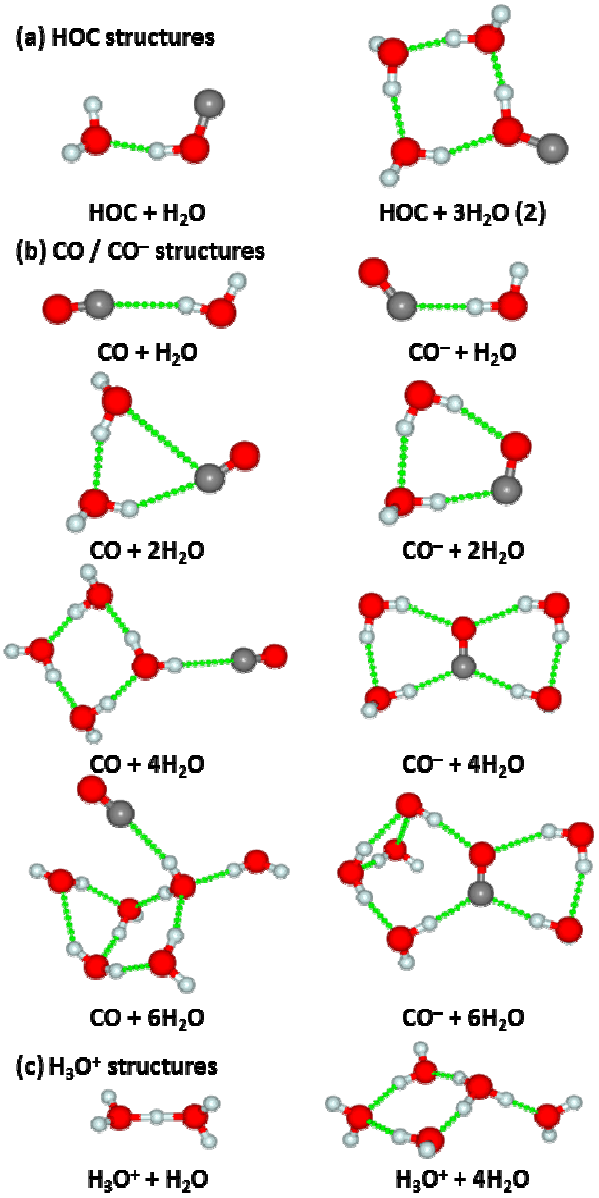

Fig. 14

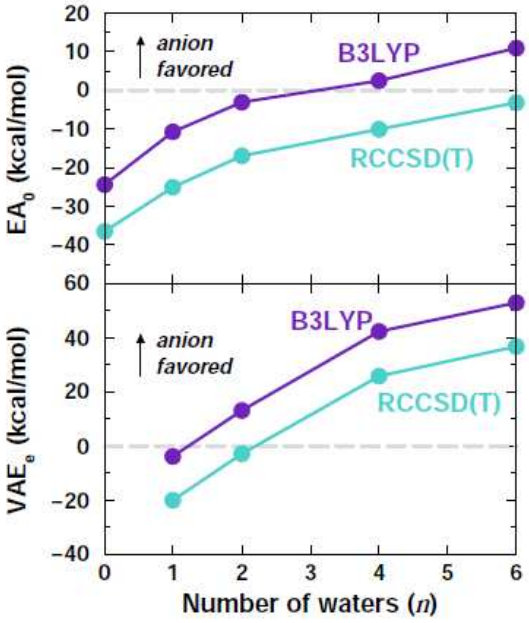

Table of Contents Graphic